Geochemistry, Geophysics, Geosystems

RESEARCH ARTICLE
10.1029/2018GC008065

Enhanced Himalayan Glacial Melting During YD and H1 Recorded in the Northern Bay of Bengal

Syee Weldeab[1], Carsten Rühlemann[2], Bodo Bookhagen[3,4], Francesco S. R. Pausata[5], and Fabiola M. Perez-Lua[1]

[1]Department of Earth Science, University of California, Santa Barbara, CA, USA, [2]Bundesanstalt für Geowissenschaften und Rohstoffe, Hannover, Germany, [3]Institute of Earth and Environmental Science, University of Potsdam, Potsdam, Germany, [4]Geography Department, University of California, Santa Barbara, CA, USA, [5]Department of Earth and Atmospheric Sciences, University of Quebec in Montreal, Montreal, Quebec, Canada

Key Points:
- Core sediments from the northern Bay of Bengal are a viable archive to reconstruct past changes in monsoonal and Himalayan meltwater runoff
- Weak monsoon reduces cloud cover and leads to increased radiative flux over the Himalaya and foreland areas and causes glacier mass loss
- A spatially integrated record of monsoon and Himalayan climate provides insights into regional climate dynamics

Supporting Information:
- Supporting Information S1

Correspondence to:
S. Weldeab,
sweldeab@ucsb.edu

Citation:
Weldeab, S., Rühlemann, C., Bookhagen, B., Pausata, F. S. R., & Perez-Lua, F. M. (2019). Enhanced Himalayan glacial melting during YD and H1 recorded in the northern Bay of Bengal. *Geochemistry, Geophysics, Geosystems*, *20*, 2449–2461. https://doi.org/10.1029/2018GC008065

Received 6 NOV 2018
Accepted 16 APR 2019
Accepted article online 1 MAY 2019
Published online 29 MAY 2019

Abstract Ocean-land thermal feedback mechanisms in the Indian Summer Monsoon (ISM) domain are an important but not well understood component of regional climate dynamics. Here we present a $\delta^{18}O$ record analyzed in the mixed-layer dwelling planktonic foraminifer *Globigerinoides ruber* (*sensu stricto*) from the northernmost Bay of Bengal (BoB). The $\delta^{18}O$ time series provides a spatially integrated measure of monsoonal precipitation and Himalayan meltwater runoff into the northern BoB and reveals two brief episodes of anomalously low $\delta^{18}O$ values between 16.3±0.4 and 16±0.5 and 12.6±0.4 and 12.3±0.4 thousand years before present. The timing of these events is centered at Heinrich event 1 and the Younger Dryas, well-known phases of weak northern hemisphere monsoon systems. Numerical climate model experiments, simulating Heinrich event-like conditions, suggest a surface warming over the monsoon-dominated Himalaya and foreland in response to ISM weakening. Corroborating the simulation results, our analysis of published moraine exposure ages in the monsoon-dominated Himalaya indicates enhanced glacier retreats that, considering age model uncertainties, coincide and overlap with the episodes of anomalously low $\delta^{18}O$ values in the northernmost BoB. Our climate proxy and simulation results provide insights into past regional climate dynamics, suggesting reduced cloud cover, increased solar radiation, and air warming of the Himalaya and foreland areas and, as a result, glacier mass losses in response to weakened ISM.

Plain Language Summary Indian Summer Monsoon rainfall and Himalayan glacier/snow melts constitute the main water source for the densely populated Indian subcontinent. Better understanding of how future climate changes will affect the monsoon rainfall and Himalayan glaciers requires a long climate record. In this study, we create a 13,000-year-long climate record that allows us to better understand the response of Indian Summer Monsoon rainfall and Himalayan glaciers to past climate changes. The focus of our study is the time window between 9,000 and 22,000 years ago, an episode where the global climate experienced large and rapid changes. Our sediment record from the northern Bay of Bengal and climate change simulation indicate that during episodes of weak monsoon, the melting of the Himalayan glaciers increases substantially significantly. This is because the weakening of the monsoon results in less cloud cover and, as a result, the surface receives more sunlight and causes glacier melting.

1. Introduction

Indian Summer Monsoon (ISM) precipitation, seasonal snowmelt, and Himalayan glaciers are the main components of the hydrological budget of the Indian subcontinent, home to 1.7 billion people (Bookhagen & Burbank, 2010; Smith & Bookhagen, 2018). Modern observation and proxy records reveal that the strength of ISM and size of Himalayan glaciers are sensitive to increase in greenhouse gases, aerosols, sea surface temperature (SST) in the Indian Ocean, and freshwater-induced perturbation of the Atlantic meridional overturning circulation (AMOC; Bolch et al., 2012; Brun et al., 2017; Dutt et al., 2015; Finkel et al., 2003; Immerzeel et al., 2010; Kääb et al., 2012; Kudrass et al., 2001; Pausata et al., 2011; Pratt-Sitaula et al., 2011; Sinha et al., 2005; Tierney et al., 2016). Climate models suggest that the current increase of greenhouse gas concentration strengthens the ISM (Polson et al., 2014, Wu et al., 2013). However, over the last 50 years ISM rainfall (rainfall over the Indian peninsula) declined, on average, by approximately 4.5% (38 mm/year) relative to the average rainfall of 852 mm/year between 1930 and 1960 (Gautam et al., 2009; Sinha et al., 2015), although the spatial pattern of rainfall trends is complex (Malik et al., 2016). Though it appears to be within the window of natural variability (Sinha et al., 2015), the multidecadal precipitation

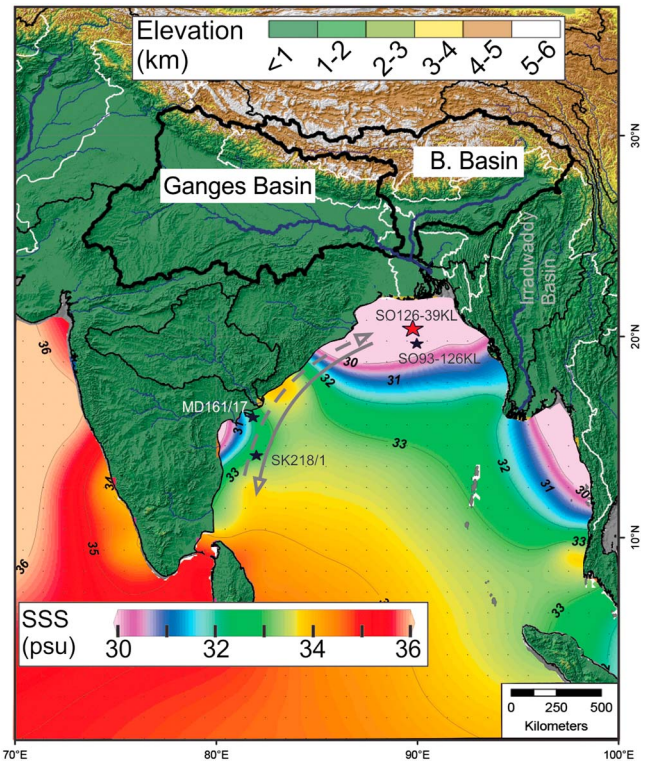

Figure 1. Oceanographic setting of the core site and topography of the GB river basin. Topographic map of the Indian Summer Monsoon domain with the Ganges and Brahmaputra (B) catchment basins indicated by bold black lines, international borders in white, and sea surface salinity (summer) of the Bay of Bengal (Zweng et al., 2013). The red star indicates the location of SO126-39KL (this study); the black stars indicate the location of SO93-126 KL (Kudrass et al., 2001), SK218/1 (Govil & Naidu, 2011), and off MD161/17 (Panmei et al., 2017). The gray arrows indicate a simplified depiction of the East India Coastal Current during summer (dashed) and winter (solid), respectively (Shankar et al., 2002).

decline is largely attributed to the influence of anthropogenic-induced increase of aerosols, suggesting that the effect of the latter on the ISM more than offsets the effect of greenhouse gas increase on the IMS (Polson et al., 2014). In contrast, over the last two decades mass loss of the Himalayan glaciers increased in response to global warming (Bolch et al., 2012; Brun et al., 2017; Finkel et al., 2003; Immerzeel et al., 2010; Kääb et al., 2012; Singh et al., 2014). Though a seasonally consistent sampling is required to unambiguously document a trend of increased meltwater input, Singh et al. (2014) suggest that the current increase of meltwater has a measurable $\delta^{18}O$ signature in the northern Bay of Bengal (BoB) surface water. While it is known that the ISM is controlled by large-scale ocean-atmosphere interaction in the tropical Indo-Pacific Ocean (Chakraborty et al., 2006), changes in the latent and sensible heat flux over the Himalayan mountains and foreland provide feedback mechanisms between Himalayan climate and the ISM (An et al., 2015). Understanding these feedback mechanisms and their contribution to regional climate changes at decadal to millennial time scales is important, but their evaluation remains challenging and debated (An et al., 2015).

The last deglacial period was punctuated by millennial-scale returns to near glacial conditions, providing an opportunity to study the response of regional climate to rapidly changing climate forcings and the interaction between the ISM and Himalayan environmental conditions. Reconstructions of surface exposure ages reveal the sensitivity of Himalayan glaciers to deglacial climate changes that, for instance, modulated the moisture supply by the Asian monsoon system (Amidon et al., 2013; Finkel et al., 2003; Pratt-Sitaula et al., 2011). Extrapolating catchment-scale Himalayan glacier reconstructions to a regional scale is, however, compounded by valley hypsometry- and longitude-dependent disparate responses of Himalayan glaciers (Amidon et al., 2013, Finkel et al., 2003, Pratt-Sitaula et al., 2011). Glacial-interglacial- and stadial-interstadial-scale reconstructions of changes in Ganges-Brahmaputra river (GBR) and Irrawaddy runoff extracted from BoB sediment sequences provide spatially integrated insights into ISM variability (Gebregiorgis et al., 2016; Govil & Naidu, 2011; Kudrass et al., 2001; Marzin et al., 2013; Rashid et al., 2011; Saraswat et al., 2013; Sijinkumar et al., 2016). However, relative to the GBR mouth, the core location of available records is likely not close enough to fully capture meltwater signatures and disentangle them from monsoonal imprints.

In this study, we present proxy-based evidence for centennial-scale episodes of enhanced meltwater input from the GBR catchment into the northern BoB at times of freshwater-induced North Atlantic surface water cooling and weakened ISM phases. The results of our modeling study suggest that a weakening of the ISM has a strong impact on the radiative budget at high elevations and, as a result, on the extent of Himalayan glaciers.

2. Study Area

The northern BoB presents a unique repository of a spatially integrated record of monsoonal rainfall and Himalayan meltwater runoff from the GBR that drains a large part of the ISM domain including the southern flank of the central and eastern Himalaya (Figure 1). The GBR runoff varies annually between 1,067 and 813 km^3/year as well as seasonally, with 161±73 km^3 and 1,451±774 km^3 during the dry (January–March) and the ISM season (July-September), respectively (Hasson et al., 2013). Though the spatial and temporal variation is significant, the glacier meltwater (snowmelt) contribution to the annual Brahmaputra (620±57 km^3) and Ganges (320±77 km^3) runoff is estimated at 15.9% (9%) and 11.5% (8.6%), respectively (Bookhagen & Burbank, 2010; Hasson et al., 2013; Lutz et al., 2014). Precipitation and evaporation over

Table 1
Radiocarbon and Calendar Age of Globigerinoides ruber s.s. and sacculifer in samples from SO126-39KL

Lab code	Sampling interval (cm)	Material	14C age (year) and uncertainty	2σ cal age range kyr (BP)	Median probability cal age (kyr, BP)
KIA 37759	170–177	*G. ruber* and *sacc*	8,685 ± 45	9–9.5	9.2
KIA 37760	205–207	*G. ruber* and *sacc*	9,815 ± 45	10.3–11	10.7
KIA 37761	265–267	*G. ruber* and *sacc*	10,830 ± 45	11.7–12.6	12.2
KIA 37762	325–330	*G. ruber* and *sacc*	11,975 ± 55	13.1–13.7	13.4
KIA 37763	345–350	*G. ruber* and *sacc*	12,690 ± 55	13.8–14.8	14.2
OS-126759	381–385	*G. ruber* and *sacc*	13,300± 55	14.8-15.7	15.2
KIA 37764	435–440	*G. ruber* and *sacc*	14,310 ± 70	16.3–17.2	16.7
KIA 37765	685–687	*G. ruber* and *sacc*	16,360 ± 90	18.8–19.5	19.2

Note. Also shown is the upper and lower ranges of the calendar age (2σ) of each radiocarbon age.

the northern BoB are estimated at 2,200 and 880 mm/year, respectively (Midhun et al., 2013; Sengupta & Sarkar, 2006; Singh et al., 2014). Relative to the southern and central BoB, the enormous amount of runoff from the GBR as well as from local rivers and precipitation over the northern BoB lowers the surface salinity (28-32 practical salinity unit) and $\delta^{18}O$ values (-2.5 to -1.5‰) of northern BoB surface water, resulting in a positive hydrologic balance (precipitation + runoff − evaporation) and a strong stratification of the upper 11–40 m of the water column (Achyuthan et al., 2013; Delaygue et al., 2001; Li et al., 2017; Midhun et al., 2013; Sengupta & Sarkar, 2006). The contribution of runoff to the salinity lowering is about 6 times larger than the precipitation over the northern BoB. The East India Coastal Current and its seasonal reversal is estimated to transport 3×10^5 km^3/year water mass, roughly 10 times more than the runoff, in and out of the BoB during the summer and winter season, respectively (Shankar et al., 2002). Between November and January, a southward flow of East India Coastal Current (0- to 55-m depth) moves low-salinity water out of the bay (Shankar et al., 2002) and is replaced by upward pumping of saline subsurface water. Although the vertical mixing is considered a major mechanism for maintaining BoB salinity (Vinayachandran et al., 2013), the extremely low surface salinity in the northern BoB (Figure 1) indicates that the intensity of vertical mixing is likely suppressed by a relatively stable salinity stratification (Parampil et al., 2010). As a result, a large amount of riverine runoff, precipitation over the northern BoB, and weak vertical mixing lead to extremely low salinity and relatively low stable oxygen isotope ($\delta^{18}O$) values of surface water (Achyuthan et al., 2013; Delaygue et al., 2001; Midhun et al., 2013; Sengupta & Sarkar, 2006). Past change in the $\delta^{18}O$ signature of northern BoB surface water is archived in the tests of mixed layer-dwelling planktonic foraminifers and, thus provide a key tool for the reconstruction of regional hydroclimate changes.

3. Materials and Methods

Sediment core SO126-39KL was recovered from the center of the runoff-induced low salinity plume in the northern BoB (20°12.4′N/89°42.5′E, 318-m water depth; Figure 1). The age model of SO126-39KL is constrained by 8 radiocarbon dates analyzed in mixed planktonic foraminifers (*Globigerinoides ruber* and *Globigerinoides sacculifer*, test size of 250-400 μm) at the Leibnitz Institute for Radiometric Dating and Isotope Research, Kiel (Germany), and at the National Ocean Sciences AMS Facility, Woods Hole (USA; Table 1). Radiocarbon dates are converted to calendar ages using Calib7.01 version (Stuiver & Reimer, 1993), the Marine13 data set (Reimer et al., 2013), and a regional reservoir correction ΔR of 76±120 years (Dutta et al., 2001; Southon et al., 2002). Uncertainties associated with the analysis of radiocarbon and the conversion of radiocarbon ages to calendar ages under the assumption of temporally constant reservoir age cumulatively contribute to the age model uncertainty of up to ±0.4 kyr. While assessing a potential temporal variation of the reservoir age in the northern BoB is not possible, the use of mixed layer-dwelling *G. ruber* and *G. sacculifer* (0-50 m) for ^{14}C-dating and the relatively weak mixing between the upper and deeper part of the water column, as suggested by the overall relatively negative $\delta^{18}O$, may reduce large changes in the reservoir age of northern BoB surface water. Nonetheless, our inability to assess a possible temporal variation of the reservoir age of northern BoB surface water posits a caveat in the age model. We constructed two age models for comparison. First, using the calendar age control points and the associated 2σ error estimates (Table 1), we created an age model based on a polynomial fit of all age model control points (Figure 2c). Clearly, this approach has a smoothing effect on the reconstructed sedimentation rate that

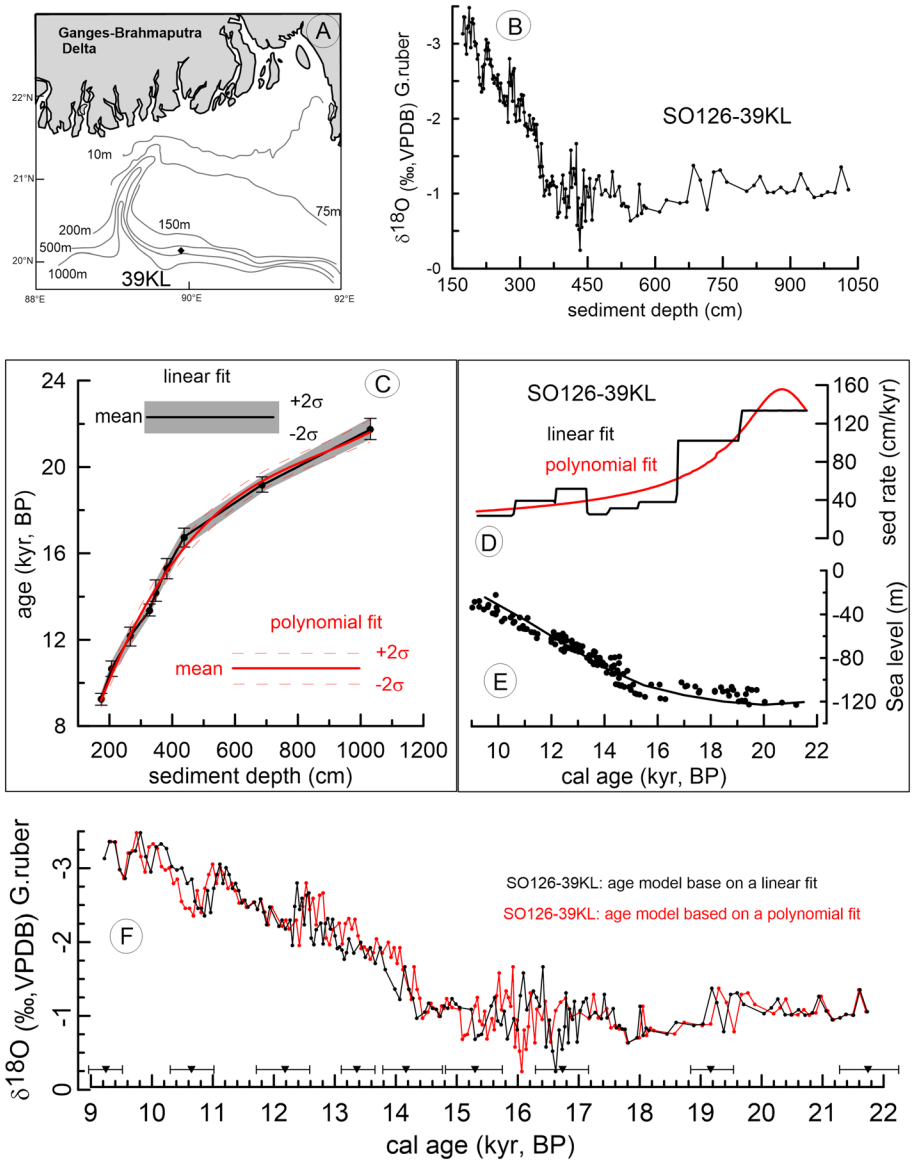

Figure 2. Setting, age model and the proxy record of SO126-39KL. (a) Bathymetric setting of SO126-39KL site. (b) $\delta^{18}O_{G\ ruber}$ record of SO126-39KL plotted versus sediment depth. (c) Age models based on polynomial (red line) fit of all age model control points (black dots with vertical black lines indicate 2σ error estimates) and linear fit between two adjacent age control points (bold black line and gray area indicates a mean age and 2σ error estimates, respectively). (d) Sedimentation rate (cm/year) calculated using age models based on the linear (black line) and polynomial fits (red curve). (e) The black line and black dots indicate global sea level changes derived from benthic foraminiferal $\delta^{18}O$ (Waelbroeck et al., 2002) and relative sea level changes based on compiled coral data (Clark et al., 2009; Deschamps et al., 2012), respectively. (f) The $\delta^{18}O_{G\ ruber}$ record of SO126-39KL plotted versus age models based on linear and polynomial fits. Triangles along the *x* axis indicate age control points and their 2σ uncertainty estimates.

gradually declines parallel to the trend of global sea level rise (Figures 2d and 2e). Second, we established an age model that is based on a linear fit between two adjacent age control points (Figures 2c). In this age model, we assume a constant sedimentation rate between two adjacent age control points. The $\delta^{18}O$ analysis of 17-22 individuals of finely crushed, well-homogenized tests of *Globigerinoides ruber sensu stricto* (250-300 um) was carried out using a Stable Isotope Ratio Mass Spectrometer MAT253 online coupled to Kiel IV (carbonate sample preparation device) at the University of California at Santa Barbara. $\delta^{18}O$ data are reported in the Vienna Pee Dee Belemnite scale with an analytical uncertainty of 0.07‰. The low abundance of *G. ruber s.s.* due to dilution by an extremely high sedimentation rate of terrigenous

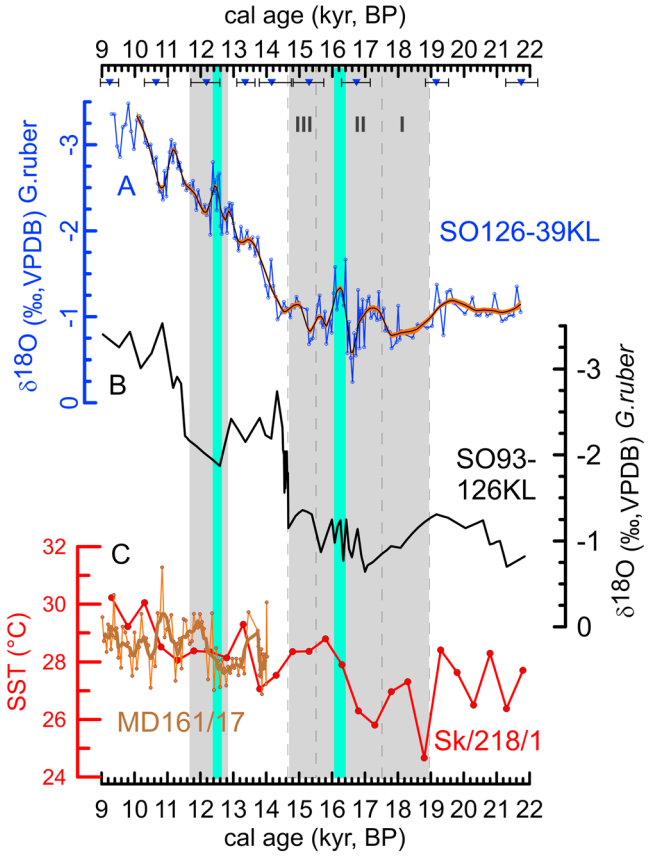

Figure 3. Comparison of SO126-39KL record to records of adjacent cores. (a) $\delta^{18}O$ of *G. ruber sensu stricto* tests analyzed in SO126-39KL samples (this study). The triangles and horizontal lines indicate age model control points and their 2σ uncertainty estimates, respectively. The thin black line shows a smoothed trend obtained using a localized regression function (loess fitting); color shading provides 2σ uncertainty estimates based on Monte Carlo simulations (10^3 runs around the smoothed trend line). (b) The strongly smoothed $\delta^{18}O_{G.\ ruber}$ record (SO93-126KL) of Kudrass et al. (2001); note only a smoothed record is available). (c) Time series of sea surface temperature (SST) estimates based on Mg/Ca analysis in *G. ruber* from the Bay of Bengal. The SST record of Govil and Naidu (2011) is indicated by a red line and the SST record of Panmei et al. (2017) is indicated by an orange line (brown line: 5-point-running average). Mg/Ca is converted to SST estimates using the equation of Gray et al. (2018), and salinity and pH effects are assessed using the approach developed by Gray and Evans (2019). The timing and duration of the Younger Dryas and Heinrich event 1 events are indicated by gray bars. Roman numerals indicate phases of Heinrich event 1 as defined by Stanford et al. (2011). The green bars indicate intervals of prominent negative $\delta^{18}O$ values in SO126-39KL within episodes of weak ISM phases.

sediments and postdepositional precipitation of coatings (most likely Fe-Mn-hydroxides) does not allow a robust foraminiferal trace element analysis.

We performed a simple isotope ($\delta^{18}O$) mass balance calculation with the aim to provide a conceptual understanding of how changes in runoff from low-to-mid altitude (0-2200 m) ISM precipitation and glacial/snow meltwater affect the isotope composition of the northern BoB mixed layer. We consider the volume of five water masses and their $\delta^{18}O$ signatures as major components that shape the $\delta^{18}O$ of northern BoB mixed layer ($\delta^{18}O_{mixed\ layer}$). Those five components are runoff from meltwater, runoff from monsoon rainfall over the low-to-middle altitude (<2200 m), precipitation over the northern BoB, evaporation from the northern BoB, and advection of water masses from eastern, central, and western BoB into the northern BoB mixed layer (40 m). By varying the runoff volume of low-mid altitude (including the precipitation over the northern BoB) and meltwater and their isotope composition systematically and keeping all other parameters constant (see Table S1 in the supporting information), we explored scenarios that would give rise to the reconstructed $\delta^{18}O_{mixed\ layer}$ of the Younger Dryas (YD) the Heinrich event 1 (H1) anomalies. The details, equations, assumptions, and caveats of the mass balance calculation are extensively discussed in the SM.

To better understand the climate dynamics associate with Heinrich 1 and its effect on the ISM, we use the model results from Pausata et al. (2011) in which the Community Atmospheric Model version 3 (CAM3; Collins et al., 2006] is employed to simulate the Last Glacial Maximum (LGM) and a Heinrich-like event. CAM3 has a horizontal resolution of roughly 2.8° by 2.8° (T42), and it has 26 vertical levels. As a starting point, the model uses insolation, carbon dioxide concentration, ice sheets, and continental geometry of the LGM, SST, and sea ice from the coupled simulation performed by Otto-Bliesner et al. (2006), which followed the Paleoclimate Model Intercomparison Project phase II protocol. A second experiment was performed in which SST is prescribed from a coupled simulation in which freshwater is abruptly added to the North Atlantic to mimic an H-event (H1), causing an extensive expansion of sea ice in the northern North Atlantic (Bitz et al., 2007). Bitz et al. (2007) added a 16-Sv-year volume of freshwater to the upper 970 m of the North Atlantic and Arctic Ocean to the control LGM simulation. The freshwater input caused a drop in salinity of 2 psu. The uncoupled experiments (LGM and H1) were run for 15 years.

We synthesized previously compiled and published ^{10}Be moraine surface exposure ages from the GBR catchment (Amidon et al., 2013; Heyman et al., 2011). We applied standardized production rates (Amidon et al., 2013), removed sample sites with large uncertainties following descriptions in Amidon et al. (2013) and use Kernel probability distribution function with a smoothing window of 0.5 kyr to synthesize moraine ages within the Himalayan GBR catchments. Figure S4 in the supporting information provides information about the age uncertainty and latitudinal distribution of the ^{10}Be moraine surface exposure ages. Based on these data and in combination with digital topographic information, we calculated the equilibrium line altitude (ELA) and the size of glaciated areas for discrete time intervals.

4. Results

At our site, millennial-to-orbital scale change in bulk sediment accumulation is likely controlled by the gradual and occasionally rapid rise in global deglacial sea level change (Deschamps et al., 2012; Waelbroeck

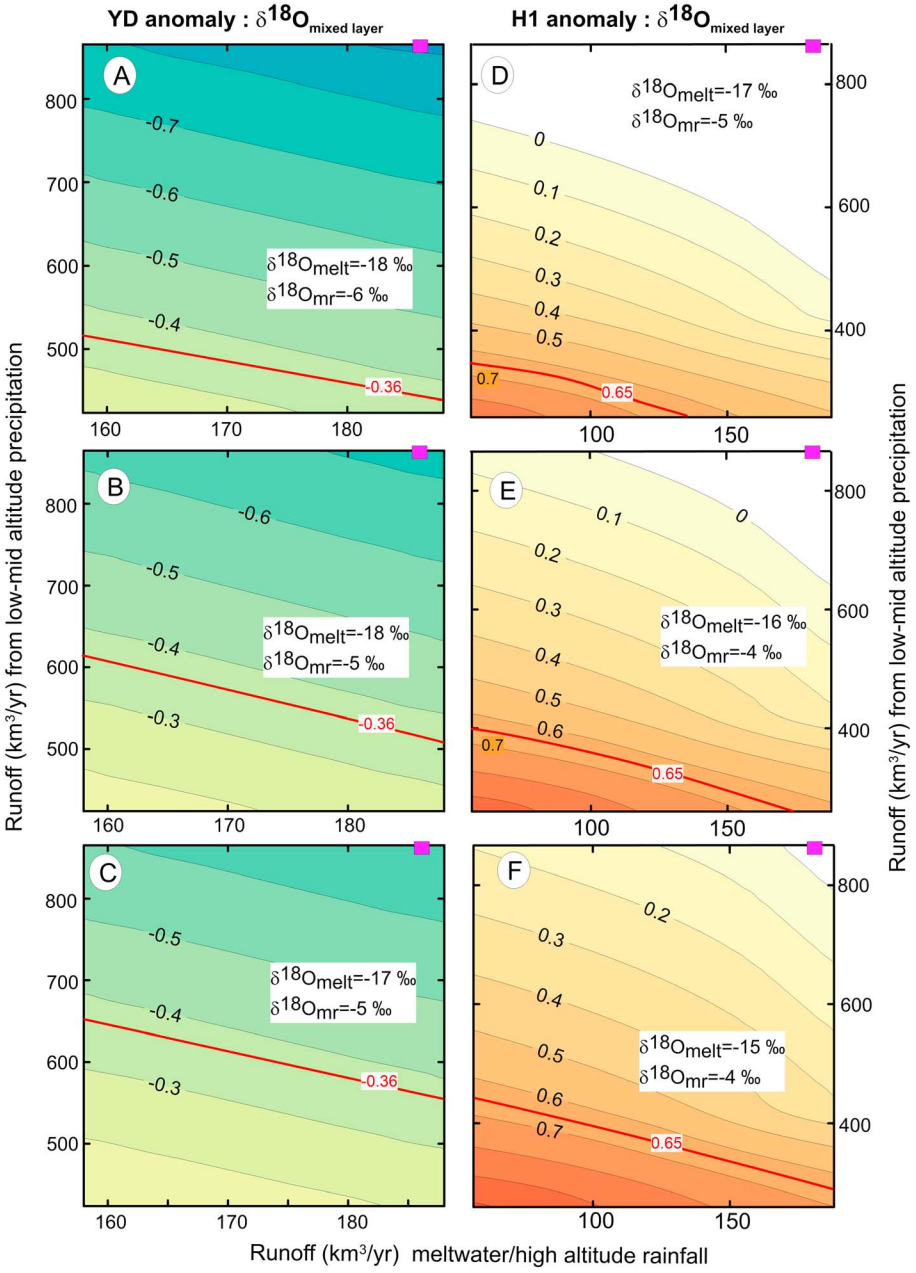

Figure 4. Results of a simple isotope mass balance calculation showing variation of $\delta^{18}O$ in the northern Bay of Bengal mixed layer ($\delta^{18}O_{mixed\text{-}layer}$) as a function of changes in monsoonal (0- to 2,200-m elevation) and Himalayan melt-water (>2,500-m elevation) runoff and the isotope composition of monsoonal ($\delta^{18}O_{mr}$) and Himalayan meltwater ($\delta^{18}O_{melt}$) runoff. (a–c and d–f) Different scenarios during Younger Dryas (YD) and Heinrich event 1 (H1) $\delta^{18}O$ anomalies, respectively. The depth of mixed layer is assumed to be 40m. The red contour line indicates the reconstructed $\delta^{18}O$ value of northern Bay of Bengal mixed layer ($\delta^{18}O_{mixed\text{-}layer}$) during the YD and H1 anomalies. $\delta^{18}O_{mixed\text{-}layer}$ (red contour line) is calculated using the average value of the negative $\delta^{18}O_{G.\ ruber}$ peaks within the YD and H1 intervals and Bay of Bengal sea surface temperature (SST) using Mg/Ca data from Govil and Naidu (2011). The magenta square on the upper left corner of each figure indicates the average monsoonal (865 km^3/year) and meltwater (188 km^3/year) runoff of the last 60 years. More parameters used in the calculation, assumption, and caveats are provided and discussed in the SM.

et al., 2002). Changes in sediment load due to rapid changes in precipitation and vegetation cover over the catchments also likely contribute to variation in sediment accumulation rate over the core location. The calculated sedimentation rate dropped abruptly and significantly at 16.8 kyr before present (BP; Figure 2d) most likely related to a combination of actual changes in sedimentation rate and an artifact

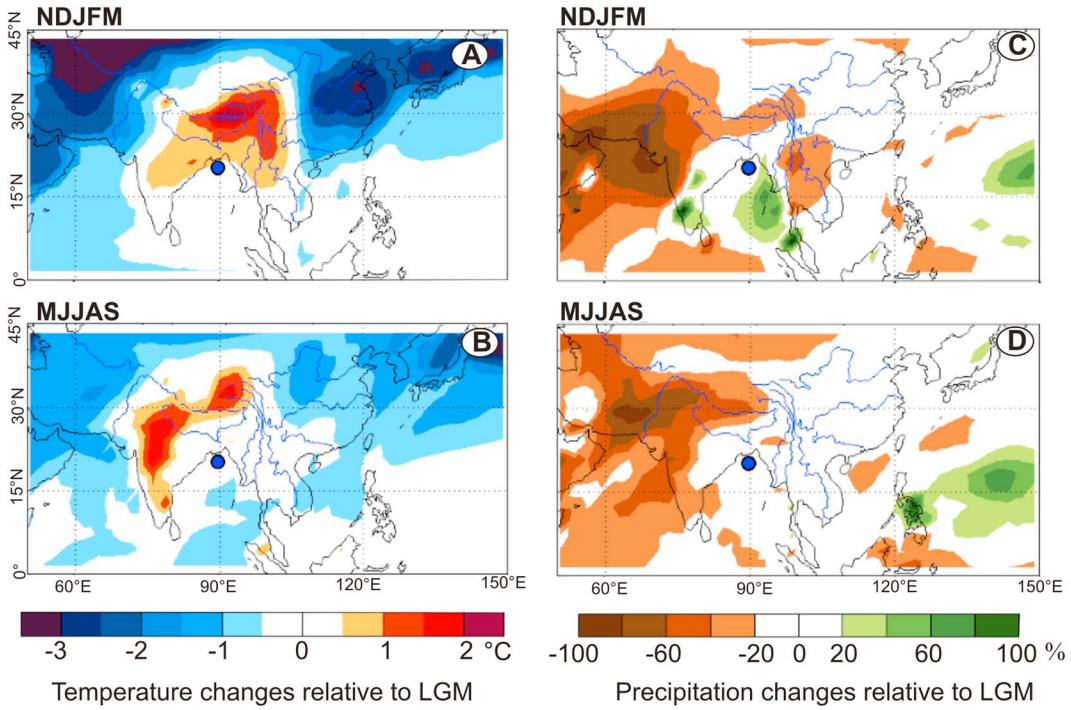

Figure 5. Results of a model simulation from Pausata et al. (2011). Average land surface temperature (left panel) and precipitation (right panel) difference between Heinrich event 1 (H1) and Last Glacial Maximum (LGM) for the period between November to March (upper panel) and May to September (lower panel). The blue marker indicates the SO129-39KL site.

associated with the assumption of a constant sedimentation rate between two adjacent age control points. We compare both the polynomial and linear fit models and, considering an age model uncertainty of ± 0.4 kyr, the results of both models are fairly similar. Because it is more likely that the linearly fitted age model is able to capture rapid sediment accumulation changes, we use this age model.

The $\delta^{18}O_{G.ruber}$ record of SO126-39KL presents a composite imprint of changes in global ice volume, riverine runoff, precipitation and evaporation over the northern BoB, and calcification temperature of *G. ruber*. Between 21.7±0.5 and 14.2±0.4 kyr BP, the $\delta^{18}O_{G.ruber}$ varies between -0.24 and -1.67‰ with an average value of -0.99±0.25‰ (n=79). Following a rapid decline at 14.2±0.4 kyr BP, $\delta^{18}O_{G.ruber}$ decreases continuously and reaches an average value of -3.16±0.18‰ (n=16) in the early Holocene. The LGM-early Holocene changes in $\delta^{18}O_{G.ruber}$ account for -2.06‰ (Figure 3). Superimposed on the orbital-to-millennial scale deglacial trend, the $\delta^{18}O_{G.ruber}$ record reveals several centennial-scale episodes of relatively negative $\delta^{18}O$ values within the YD and H1 events (Figure 3). Here we focus on the most prominent negative $\delta^{18}O$ peak that are centered between 16.3±0.4 and 16±0.5 and between 12.6±0.4 and 12.3± 0.4 cal kyr BP. Noting that the short duration (~300 years) of the events and an age model uncertainty of ±400 years (2σ) present a caveat in pinpointing the timing of the events more precisely, the two negative $\delta^{18}O$ excursions occurred within the YD (12.9-11.6 cal kyr BP) and Heinrich event 1 (H1: 19-14.6 cal kyr BP), both prominent episodes of weakening of the northern hemisphere monsoon systems (Dutt et al., 2015; Sinha et al., 2005; Wang et al., 2001; Weldeab et al., 2007).

5. Discussion

As discussed below and summarized in a flow diagram (Figure 8), the inference of this study is that episodes of freshwater-induced weakening of the AMOC and, as a result, weakening of ISM and reduction of cloud cover caused an increased melting of Himalayan glaciers.

Our records show two prominent negative $\delta^{18}O$ anomalies (enriched in ^{16}O) that are centered at 16.3±0.4-to-16±0.5 and 12.6±0.4-to-12.3± 0.4 kyr cal BP, as highlighted in Figure 3a. The timing and duration of these

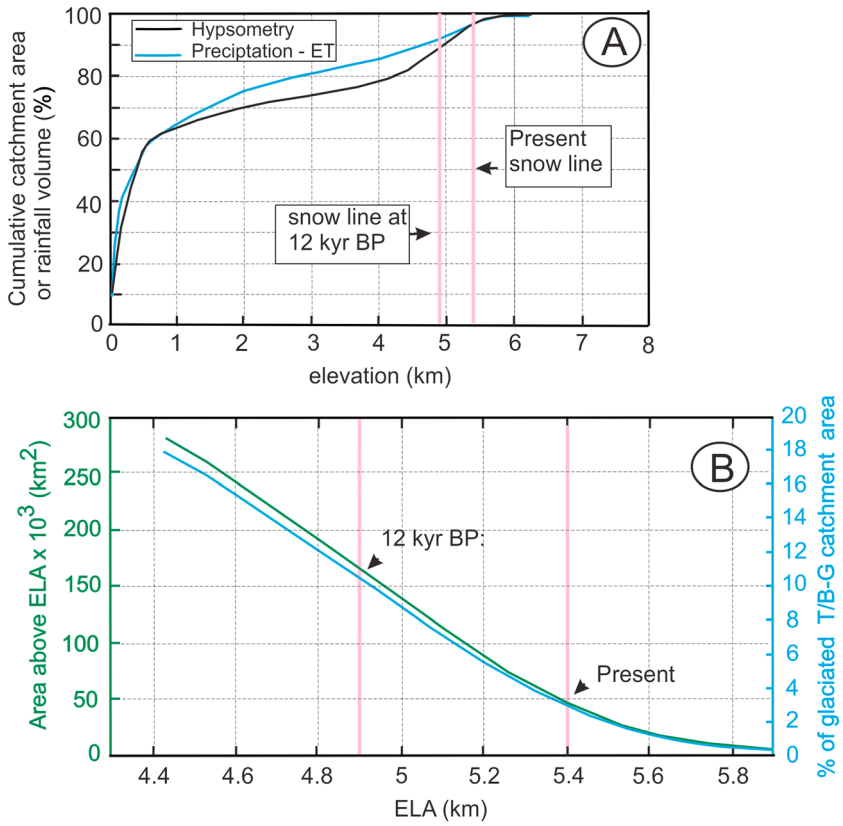

Figure 6. Changes in the position of the snow line and in the size of glaciated areas within the southern Himalayan front and the GBR basin. (a) Hypsometry and estimate of cumulative catchment area and rainfall volume below and above the equilibrium line altitude (ELA) at present and at 12 kyr BP. (b) Estimated glaciated area at southern Himalayan front at 12 kyr BP. The green line indicates the area above the ELA, and blue line indicates the percentage glaciation of the Ganges-Brahmaputra catchment (b).

two events are well constrained by relatively narrowly spaced age model control points (Figure 2 and Table 1). During the two $\delta^{18}O$ events, the rate of sediment accumulation does not show large changes, indicating the absence of an allochthonous sediment contribution. This is consistent with our visual examination of the core sediment. These two events occurred within well-known episodes of weak northern hemisphere monsoon systems, as indicated by strong $\delta^{18}O$ enrichment in Indian and Chinese stalagmite records (Cai et al., 2015; Dutt et al., 2015; Kathayat et al., 2016; Sinha et al., 2005; Wang et al., 2001). The weakening of the ISM during the YD and H1 is also manifested by relatively heavy $\delta^{18}O$ (enriched in ^{18}O) values in numerous BoB core sediments (Figures 3 and S1; Gebregiorgis et al., 2016; Govil & Naidu, 2011; Kudrass et al., 2001; Marzin et al., 2013; Rashid et al., 2011; Sijinkumar et al., 2016]. We compare our $\delta^{18}O_{G.\ ruber}$ record with that of SO93-126KL, which is located 42 km southeast of our site (Figures 1 and 3b; Kudrass et al., 2001]. On a millennial scale, the comparison indicates that the onset of the Bølling-Allerød in SO126-39KL is delayed by 0.4 kyr relative to that of SO93-126KL. Noting that the lag of 0.4 kyr is within the uncertainty of the age model, we do not assume that there is a climate lead-lag pattern between the sites with regard to the onset of Bølling-Allerød. In contrast to the gradual increase of $\delta^{18}O$ after the early phase of the Bølling-Allerød and abrupt $\delta^{18}O$ increase during the YD, as recorded in stalagmites and sediments from the central and southern BoB (Figures 3 and S1), the $\delta^{18}O$ record of SO93-39KL (this study) shows a continuous enrichment of ^{16}O (negative $\delta^{18}O$ value) until 11 kyr BP (Figure 3). This observation indicates that in addition to the monsoonal runoff and mixed layer temperature increase, the deglacial $\delta^{18}O$ record in the northernmost BoB is strongly modulated by a centennial-scale glacier meltwater input with an extremely low $\delta^{18}O$ signature (Singh et al., 2014). Because only a strongly smoothed $\delta^{18}O_{G.\ ruber}$ record of SO93-126KL is available (Figure 3), we limit our centennial scale comparison to the H1 interval where the smoothing appears to have less effect on the

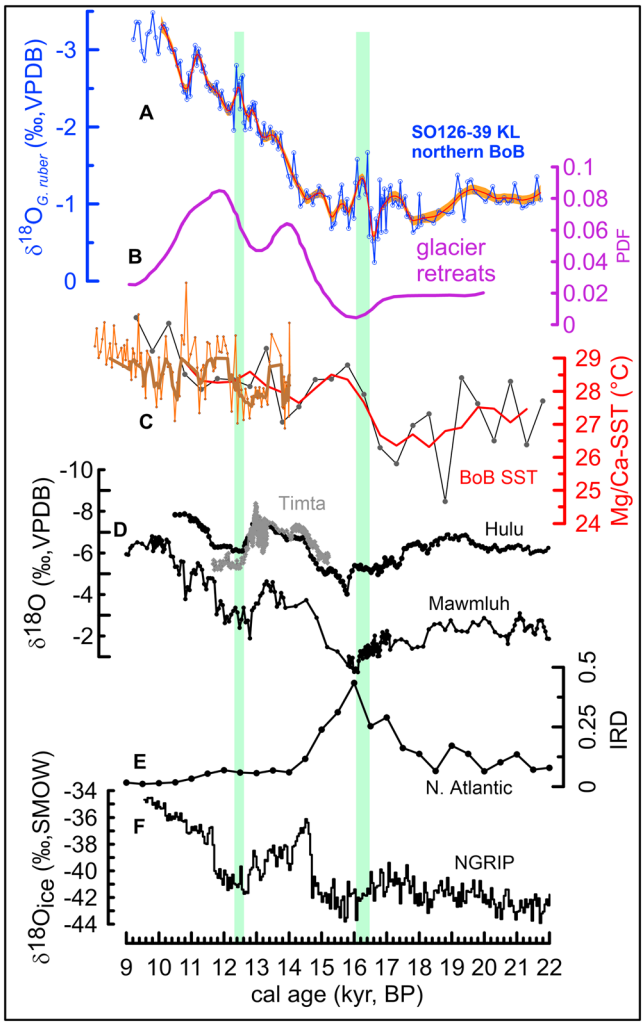

Figure 7. Comparison of SO126-39KL record with records from the ISM and Asian monsoon domains and the northern high latitude. (a) The $\delta^{18}O_{G.ruber}$ record of SO126-39KL. The thin black line shows a smoothed trend obtained using a localized regression function (loess fitting); color shading provides 2σ uncertainty estimates based on Monte Carlo simulations (10^3 runs around the smoothed trend line). (b) Kernel probability density function (with a smoothing window of 0.5 kyr) of ^{10}Be exposure surface ages compiled from sites within the Ganges and Brahmaputra catchment (see AM for more details). (c) As in Figure 3c. (d) $\delta^{18}O$ record of stalagmites Hulu (Wang et al., 2001), Mawmluh (Dutt et al., 2015), and Timta (Sinha et al., 2005) caves. (e) Stacked record of ice rafted detritus (IRD, arbitrary unit) from the North Atlantic (Stern & Lisiecki, 2013). (f) $\delta^{18}O$ record of NGRIP (NGRIP-members, 2004).

centennial scale features (Figure 3). While during H1 the millennial scale $\delta^{18}O_{G.\ ruber}$ trend in both SO93-126KL and SO126-39KL records is similar, on centennial scale an outstanding negative $\delta^{18}O$ peak in the SO93-126KL record is not developed (Figure 3). In SO126-39KL (this study), relative to the immediately preceding intervals, the magnitude of centennial-scale $\delta^{18}O_{G.ruber}$ decrease within the YD and H1 accounts for 0.5 ‰ (n=7) and 0.7 ‰ (n=7), respectively. If the $\delta^{18}O$ decrease were solely caused by SST changes, it would require a centennial scale mixed layer warming by 2 and 3.5°C during YD and H1, respectively. The resolution of available temperature reconstructions of the BoB mixed layer is insufficient to unravel centennial-scale changes in SST (Figure S2; Gebregiorgis et al., 2016; Govil & Naidu, 2011; Kudrass et al., 2001; Saraswat et al., 2013). The $\delta^{18}O$ record of SO93-126KL does not support a warming of 3.5 and 2°C during YD and H1, respectively. A relatively well resolved BoB SST record covering the YD (but not H1) suggests a 1°C increase during the second half of the YD episode and the warming persists throughout the early Holocene (Panmei et al., 2017; Figure 3c). The timing, magnitude, and duration of the warming are inconsistent with the pattern of the centennial scale anomalously negative $\delta^{18}O$ peak in our record. For instance, while the onset of SST rise overlaps with the end of the negative $\delta^{18}O$ anomalies during YD, the SST persists at an elevated level when the $\delta^{18}O$ abruptly increases (Figure 3c). This discrepancy indicates that the SST trend in the Panmei et al. (2017) record is not the dominant factor that shaped the centennial scale anomalously negative $\delta^{18}O$ event in the northernmost BoB.

Culture experiments and field observations (Bijma et al., 1990; Ufkes et al., 1998) indicate that the abundance and survival of *G. ruber* white are dramatically reduced in extremely low salinity environments. A weakening of the ISM during the YD and H1, as indicated by several terrestrial and marine (northern BoB) $\delta^{18}O$ records, reduces riverine runoff into the northern BoB and shrinks the depth of an extremely low salinity layer to few meters of the surface water and, as result, expands the mixed layer upward, as indicated by modern observations (Li et al., 2017). Based on the above factors, we argue that the anomalously low $\delta^{18}O$ values within H1 and YD are unlikely to reflect a shift of *G. ruber* habitat depth to a very narrow range and extremely shallow depth. Instead we hypothesize that the most likely scenario for the significantly low $\delta^{18}O$ values within the episodes of H1 and YD is an increase of Himalayan meltwaters (extremely low $\delta^{18}O$ values) and a simultaneous decrease of monsoonal runoff in response to a ISM weakening. Relative to the isotope composition of ISM precipitation over low-to-mid elevations (<2,200 m) and ISM precipitation over the BoB with an average $\delta^{18}O$ value of -7.4±2,5‰ and -5‰, respectively (Breitenbach et al., 2010; Sengupta & Sarkar, 2006), the $\delta^{18}O$ signature of snow and glacier meltwater over the east-west trending Brahmaputra drainage basin (4- to 5-km elevation) is significantly negative and varies between -21 and -13‰ (Hren et al., 2009; Yao et al., 2013). To test our hypothesis, we performed a simple oxygen isotope mass balance calculation. Because of the several assumptions we had to make and the uncertainty associated with the assumptions, the results of our mass balance calculation should be considered as a semiquantitative estimate. Consistent with our hypothesis, a key feature of all scenarios is that in order to obtain the reconstructed $\delta^{18}O_{mixed\text{-}layer}$ values, the decrease of low-to-mid elevation monsoonal precipitation must be accompanied by a relative increase of meltwater runoff (Figure 4). The impact of meltwater on the $\delta^{18}O_{mixed\text{-}layer}$ values primarily arises from the extremely low $\delta^{18}O$ value of the meltwater, while the volumetric increase of the meltwater is

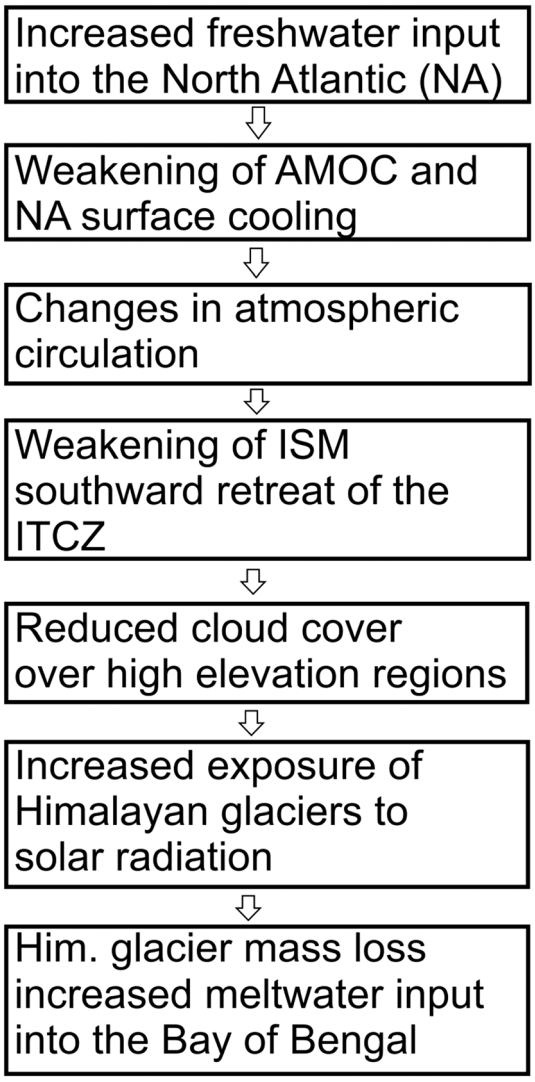

Figure 8. A flow diagram illustrating the inferred sequence of events that start with a freshwater-induced AMOC weakening and North Atlantic surface cooling during Heinrich event 1 (H1) and Younger Dryas (YD).

relatively small compared to the runoff decrease of the low-to-mid elevation monsoonal rainfall (Figure 4).

To explore underlying physical causes for our proxy observation, we analyzed the model simulations used in Pausata et al. (2011). The results of the simulation show a decline of precipitation and warming over the high elevations of the GBR catchment in both summer and winter (Figure 5) during archetypal Heinrich events relative to the LGM. Though limited to southeastern India, another H1-like hosing experiment (Marzin et al., 2013) also indicates summer warming. The winter warming is due to the weakening of the winter monsoon in the H1 experiment compared to the LGM experiment, which is associated with the cooling of Arabian Sea surface water (Pausata et al., 2011; Tierney et al., 2016) and leads to anomalous warm advection into northern India (Pausata et al., 2011). The summer warming is related to a reduced cloud cover (weak ISM) and therefore increased radiation affecting the surface energy budget (Mölg et al., 2012; Rupper & Roe, 2008). Summer warming is essential to expanding the seasonal snow-melt regime and enhancing snow and glacier meltwater that would have downstream impacts on the $\delta^{18}O$ signature of northern BoB surface water, providing a viable mechanism for our observation.

To further test our hypothesis of increased meltwater input, we compiled published ^{10}Be moraine surface exposure ages from the GBR catchment (Amidon et al., 2013; Heyman et al., 2011) and calculated the ELA and the size of glaciated areas for discrete time intervals (Figure 6). Because of the steep elevation-area relation in the Himalaya, elevation changes of the ELA of a few hundred meters have a large impact on the glaciated area of the Himalaya (Figure 6). For example, the downward shift from the present-day ELA at 5.4 km to the 12-kyr BP ELA at 4.9-km elevation increases the area above the ELA fourfold from 45.3 $\times 10^3$ km^2 to 165.2 $\times 10^3$ km^2 (Figure 6). This supports significantly larger glaciers and causes significant runoff during glacial melting.

The synthesized ^{10}Be moraine surface exposure ages indicate that the timing of hypothesized meltwater spikes during the YD fall within the time windows of an increasing glacier recession in the GBR catchment south of the orographic barrier (Figure 7). While the interval of low $\delta^{18}O$ centered at 16.3±0.4 and 16±0.5 kyr BP falls within a phase of reduced glacier retreat over the GBR catchment south of the orographic barrier (Figure 7), ^{10}Be data from region north of orographic barrier (within the GBR catchment) and the Indus catchment indicate glacier retreats during H1 (Figure S4b). While the Indus catchment does not contribute to the runoff input into the BoB, it is likely that the coarse temporal and spatial resolution of the moraine records and the significant dating uncertainty of the ^{10}Be surface exposure ages fail to unravel all episodes and sites of enhanced activities of GBR catchment glaciers. Noting the above uncertainty, our calculation indicates that at 12 kyr BP the ELA was located at an elevation of 4,900 m (Figure 6). Consequently, an area of 165$\times 10^3$ km^2, which makes 10.5% of the total GBR basin, was glaciated and approximately 8% of the total precipitation volume occurred above the ELA (Figure 6). Relative to the present with an ELA of ~5,400 m and a glaciated area of 45.3$\times 10^3$ km^2 or 2.9% of the total GBR catchment, the glaciated area during YD and most likely during H1 was substantially larger. As a result, the amount of meltwater input during the two short episodes within the YD and H1 could have been significantly increased during elevated summer temperature, as suggested by the results of our simulation. Noting age model uncertainty and the brief duration of the events, the key finding of our study is that the effect of weak ISM is not limited to a reduction of moisture supply to the Himalaya and foreland but also caused high-elevation warming that led to enhanced meltwaters.

Air warming over northern India and the southern Himalaya, as suggested by the results of the climate simulation, and the ISM weakening are linked to the freshwater induced AMOC weakening and, as a result, surface cooling of the northern high latitude and midlatitude (Marzin et al., 2013; NGRIP-members, 2004; Pausata et al., 2011; Shakun et al., 2012; Tierney et al., 2016). According to the results of our and previous climate simulations (Marzin et al., 2013; Pausata et al., 2011; Tierney et al., 2016), the link is established via large-scale atmospheric changes, involving a cooling of the surface temperature over the western Indian Ocean and a southward displacement of the Intertropical Convergence Zone. Figure 8 summarizes the inferred sequence of events.

6. Conclusions

Our record provides new insights into the impact of ISM weakening on the monsoon-dominated Himalaya and foreland areas. Our proxy record indicates centennial-scale episodes of an increased meltwater input into the BoB during YD and H1 episodes of millennial-scale weakening of the ISM. Corroborating the proxy-based evidence, the results of our climate model simulation suggest a surface warming of the monsoon-dominated Himalaya in response to millennial-scale ISM weakening. Our interpretation of the sequence of events is as follows (Figure 8): YD and H1 meltwater input into the North Atlantic led to a weakening of the AMOC and subsequent North Atlantic surface water cooling. The latter caused large-scale atmospheric circulation changes that led to a weakening of the ISM. A weak ISM led to reduced cloud cover in the high-elevation monsoon area and, as a result, increased radiative flux and glacier mass loss. We conclude that a weak ISM not only reduces moisture supply to glaciers but causes glacier mass loss due to an increased exposure to solar radiation. Our findings have a broader implication for understanding the dynamics of Himalayan glaciers during the last glacial and Marine Isotope Stage 3 that were punctuated by several Heinrich events that caused the ISM to weaken (Kudrass et al., 2001; Marzin et al., 2013). If surface warming over northern India and the southern Himalaya is a consistent feature of Heinrich events, as suggested for H1 in this study, then the monsoon-dominated Himalayan glaciers were likely subject to repeated advances and retreats, and this could provide a viable explanation for the scattered record of Himalayan glaciation during the LGM (Amidon et al., 2013). Our study highlights the importance of understanding glacier meltwater contributions to the marine $\delta^{18}O$ record in the BoB. The $\delta^{18}O$ data, in turn, have high potential to provide spatially integrated insights into the monsoon-dominated Himalayan climate and its thermal and hydrological response to changes in the ISM strength.

Acknowledgments
We thank Dorothy K. Pak for discussion and three anonymous reviewers for their constructive comments and suggestions. We also thank the Editor, Branwen Williams, for her handling of the manuscript. Data presented in this study are available at the NOAA Paleoclimatology date center (https://www.ncdc.noaa.gov/data-access/paleoclimatology-data) and Pangaea (pangaea.de).

References

Achyuthan, H., Deshpande, R. D., Rao, M. S., Kumar, B., Nallathambi, T., Shashi Kumar, K., et al. (2013). Stable isotopes and salinity in the surface waters of the Bay of Bengal: Implications for water dynamics and palaeoclimate. *Marine Chemistry*, *149*, 51–62. https://doi.org/10.1016/j.marchem.2012.12.006

An, Z., Guoxiong, W., Jianping, L., Youbin, S., Yimin, L., Weijian, Z., et al. (2015). Global monsoon dynamics and climate change. *Annual Review of Earth and Planetary Sciences*, *43*(1), 29–77. https://doi.org/10.1146/annurev-earth-060313-054623

Bijma, J., Faber, W. W., & Hemleben, C. (1990). Temperature and salinity limits for growth and survival of some planktonic foraminifers in laboratory cultures. *Journal of Foraminiferal Research*, *20*(2), 95–116. https://doi.org/10.2113/gsjfr.20.2.95

Bitz, C. M., Chiang, J. C. H., Cheng, W., & Barsugli, J. J. (2007). Rates of thermohaline recovery from freshwater pulses in modern, Last Glacial Maximum, and greenhouse warming climates. *Geophysical Research Letters*, *34*, L07708. https://doi.org/10.1029/2006GL029237

Bolch, T., Kulkarni, A., Kaab, A., Huggel, C., Paul, F., Cogley, J. G., et al. (2012). The state and fate of Himalayan glaciers. *Science*, *336*(6079), 310–314. https://doi.org/10.1126/science.1215828

Bookhagen, B., & Burbank, D. W. (2010). Toward a complete Himalayan hydrological budget: Spatiotemporal distribution of snowmelt and rainfall and their impact on river discharge. *Journal of Geophysical Research*, *115*, F03019. https://doi.org/10.1029/2009JF001426

Breitenbach, S. F. M., Adkins, J. F., Meyer, H., Marwan, N., Kumar, K. K., & Haug, G. H. (2010). Strong influence of water vapor source dynamics on stable isotopes in precipitation observed in Southern Meghalaya, NE India. *Earth and Planetary Science Letters*, *292*(1-2), 212–220. https://doi.org/10.1016/j.epsl.2010.01.038

Brun, F., Berthier, E., Wagnon, P., Kääb, A., & Treichler, D. (2017). A spatially resolved estimate of High Mountain Asia glacier mass balances from 2000 to 2016. *Nature Geoscience*, *10*(9), 668–673. https://doi.org/10.1038/ngeo2999

Cai, Y., Fung, I. Y., Edwards, R. L., An, Z., Cheng, H., Lee, J. E., et al. (2015). Variability of stalagmite-inferred Indian monsoon precipitation over the past 252,000 y. *Proceedings of the National Academy of Sciences*, *112*(10), 2954–2959. https://doi.org/10.1073/pnas.1424035112

Chakraborty, A., Nanjundiah, R. S., & Srinivasan, J. (2006). Theoretical aspects of the onset of Indian Summer Monsoon from perturbed orography simulations in a GCM. *Annales Geophysicae*, *24*(8), 2075–2089. https://doi.org/10.5194/angeo-24-2075-2006

Clark, P. U., Dyke, A. S., Shakun, J. D., Carlson, A. E., Clark, J., Wohlfarth, B., et al. (2009). The Last Glacial Maximum. *Science*, *325*(5941), 710–714. https://doi.org/10.1126/science.1172873

Collins, W. D., Rasch, P. J., Boville, B. A., Hack, J. J., McCaa, J. R., Williamson, D. L., et al. (2006). The formulation and atmospheric simulation of the Community Atmosphere Model Version 3 (CAM3). *Journal of Climate*, *19*(11), 2144–2161. https://doi.org/10.1175/JCLI3760.1

Deschamps, P., Durand, N., Bard, E., Hamelin, B., Camoin, G., Thomas, A. L., et al. (2012). Ice-sheet collapse and sea-level rise at the Bolling warming 14,600 years ago. *Nature*, *483*(7391), 559–564. https://doi.org/10.1038/nature10902

Dutt, S., Gupta, A. K., Clemens, S. C., Cheng, H., Singh, R. K., Kathayat, G., & Edwards, R. L. (2015). Abrupt changes in Indian Summer Monsoon strength during 33,800 to 5500 years B. P. *Geophysical Research Letters*, *42*, 5526–5532. https://doi.org/10.1002/2015GL064015

Dutta, K., Bhushan, R., & S. B.L.K. (2001). Delta R correction values for the Northern Indian Ocean. *Radiocarbon*, *43*(2A), 483–488. https://doi.org/10.1017/S0033822200038376

Finkel, R. C., Owen, L. A., Barnard, P. L., & Caffee, M. W. (2003). Beryllium-10 dating of Mount Everest moraines indicates strong monsoon influence and glacial synchroneity throughout the Himalaya. *Geology*, *31*(6), 561–564. https://doi.org/10.1130/0091-7613(2003)031<0561:BDOMEM>2.0.CO;2

Gautam, R., Hsu, N. C., Lau, K. M., & Kafatos, M. (2009). Aerosol and rainfall variability over the Indian monsoon region: Distributions, trends and coupling. *Annales Geophysicae*, *27*(9), 3691–3703. https://doi.org/10.5194/angeo-27-3691-2009

Hasson, S., Lucarini, V., & Pascale, S. (2013). Hydrological cycle over South and Southeast Asian river basins as simulated by PCMDI/CMIP3 experiments. *Earth System Dynamics*, *4*(2), 199–217. https://doi.org/10.5194/esd-4-199-2013

Hren, M. T., Bookhagen, B., Blisniuk, P. M., Booth, A. L., & Chamberlain, C. P. (2009). δ18O and δD of streamwaters across the Himalaya and Tibetan Plateau: Implications for moisture sources and paleoelevation reconstructions. *Earth and Planetary Science Letters*, *288*(1-2), 20–32. https://doi.org/10.1016/j.epsl.2009.08.041

Immerzeel, W. W., Pellicciotti, F., & Bierkens, M. F. P. (2010). Rising river flows throughout the twenty-first century in two Himalayan glacierized watersheds. *Nature Geoscience*, *6*(9), 742–745. https://doi.org/10.1038/ngeo1896

Kääb, A., Berthier, E., Nuth, C., Gardelle, J., & Arnaud, Y. (2012). Contrasting patterns of early twenty-first-century glacier mass change in the Himalayas. *Nature*, *488*(7412), 495–498. https://doi.org/10.1038/nature11324

Kathayat, G., Cheng, H., Sinha, A., Spötl, C., Edwards, R. L., Zhang, H., & Breitenbach, S. F. M. (2016). Indian monsoon variability on millennial-orbital timescales. *Scientific Reports*, *6*(1). https://doi.org/10.1038/srep24374

Li, Y., Han, W., Wang, W., Ravichandran, M., Lee, T., & Shinoda, T. (2017). Bay of Bengal salinity stratification and Indian Summer Monsoon intraseasonal oscillation: 2. Impact on SST and convection. *Journal of Geophysical Research: Oceans*, *122*, 4312–4328. https://doi.org/10.1002/2017JC012692

Lutz, A. F., Immerzeel, W. W., Shrestha, A. B., & Bierkens, M. F. P. (2014). Consistent increase in High Asia's runoff due to increasing glacier melt and precipitation. *Nature Climate Changes*, *4*(7), 587–592. https://doi.org/10.1038/NCLIMATE2237

Malik, N., Bookhagen, B., & Mucha, P. J. (2016). Spatiotemporal patterns and trends of Indian monsoonal rainfall extremes. *Geophysical Research Letters*, *43*, 1710–1717. https://doi.org/10.1002/2016GL067841

Mölg, T., Maussion, F., Yang, W., & Scherer, D. (2012). The footprint of Asian monsoon dynamics in the mass and energy balance of a Tibetan glacier. *The Cryosphere*, *6*(6), 1445–1461. https://doi.org/10.5194/tc-6-1445-2012

NGRIP-members (2004). High-resolution record of Northern Hemisphere climate extending into the last interglacial period. *Nature*, *431*, 147–151.

Otto-Bliesner, B. L., Brady, E. C., Clauzet, G., Tomas, R., Levis, S., & Kothavala, Z. (2006). Last Glacial Maximum and Holocene Climate in CCSM3. *Journal of Climate*, *19*(11), 2526–2544. https://doi.org/10.1175/JCLI3748.1

Parampil, S. R., Gera, A., Ravichandran, M., & Sengupta, D. (2010). Intraseasonal response of mixed layer temperature and salinity in the Bay of Bengal to heat and freshwater flux. *Journal of Geophysical Research*, *115*, C05002. https://doi.org/10.1029/2009JC005790

Pausata, F. S. R., Battisti, D. S., Nisancioglu, K. H., & Bitz, C. M. (2011). Chinese stalagmite $\delta^{18}O$ controlled by changes in the Indian monsoon during a simulated Heinrich event. *Nature Geoscience*, *4*(7), 474–480. https://doi.org/10.1038/ngeo1169

Polson, D., Bollasina, M., Hegerl, G. C., & Wilcox, L. J. (2014). Decreased monsoon precipitation in the Northern Hemisphere due to anthropogenic aerosols. *Geophysical Research Letters*, *41*, 6023–6029. https://doi.org/10.1002/2014GL060811

Pratt-Sitaula, B., Burbank, D. W., Heimsath, A. M., Humphrey, N. F., Oskin, M., & Putkonen, J. (2011). Topographic control of asynchronous glacial advances: A case study from Annapurna, Nepal. *Geophysical Research Letters*, *38*, L24502. https://doi.org/10.1029/2011GL049940

Reimer, P. J., Bard, E., Bayliss, A., Beck, J. W., Blackwell, P. G., Ramsey, C. B., et al. (2013). IntCal13 and Marine13 radiocarbon age calibration curves 0–50,000 years cal BP. *Radiocarbon*, *55*(4), 1869–1887. https://doi.org/10.2458/azu_js_rc.55.16947

Rupper, S., & Roe, G. (2008). Glacier changes and regional climate: A mass and energy balance approach. *Journal of Climate*, *21*(20), 5384–5401. https://doi.org/10.1175/2008JCLI2219

Sengupta, S., & Sarkar, A. (2006). Stable isotope evidence of dual (Arabian Sea and Bay of Bengal) vapour sources in monsoonal precipitation over north India. *Earth and Planetary Science Letters*, *250*(3-4), 511–521. https://doi.org/10.1016/j.epsl.2006.08.011

Shakun, J. D., Clark, P. U., He, F., Marcott, S. A., Mix, A. C., Liu, Z., et al. (2012). Global warming preceded by increasing carbon dioxide concentrations during the last deglaciation. *Nature*, *484*(7392), 49–54. https://doi.org/10.1038/nature10915

Shankar, D., Vinayachandran, P. N., & Unnikrishnan, A. S. (2002). The monsoon currents in the north Indian Ocean. *Progress in Oceanography*, *52*(1), 63–120. https://doi.org/10.1016/S0079-6611(02)00024-1

Sijinkumar, A. V., Clemens, S., Nath, B. N., Prell, W., Benshila, R., & Lengaigne, M. (2016). δ18O and salinity variability from the Last Glacial Maximum to Recent in the Bay of Bengal and Andaman Sea. *Quaternary Science Reviews*, *135*, 79–91. https://doi.org/10.1016/j.quascirev.2016.01.022

Singh, A., Mohiuddin, A., Ramesh, R., & Raghav, S. (2014). Estimating the loss of Himalayan Glaciers under global warming using the δ18O–salinity relation in the Bay of Bengal. *Environmental Science & Technology Letters*, *1*(5), 249–253. https://doi.org/10.1021/ez500076z

Sinha, A., Cannariato, K. G., Stott, L. D., Li, H. C., You, C. F., Cheng, H., et al. (2005). Variability of Southwest Indian Summer Monsoon precipitation during the Bolling-Allerod. *Geology*, *33*(10), 813–816. https://doi.org/10.1130/g21498.1

Sinha, A., Kathayat, G., Cheng, H., Breitenbach, S. F., Berkelhammer, M., Mudelsee, M., et al. (2015). Trends and oscillations in the Indian Summer Monsoon rainfall over the last two millennia. *Nature Communications*, *6*(1), 1–7. https://doi.org/10.1038/ncomms7309

Smith, T., & Bookhagen, B. (2018). Changes in seasonal snow water equivalent distribution in High Mountain Asia (1987 to 2009). *Science Advances*, *4*(1), e1701550. https://doi.org/10.1126/sciadv.1701550

Southon, J., Kashgarian, M., Fontugne, M., Metivier, B., & Yim, W. W.-S. (2002). Marine reservoir corrections for the Indian Ocean and Southeast Asia. *Radiocarbon*, *44*(01), 167–180. https://doi.org/10.1017/S0033822200064778

Stanford, J. D., Rohling, E. J., Bacon, S., Roberts, A. P., Grousset, F. E., & Bolshaw, M. (2011). A new concept for the paleoceanographic evolution of Heinrich event 1 in the North Atlantic. *Quaternary Science Reviews*, *30*(9-10), 1047–1066. https://doi.org/10.1016/j.quascirev.2011.02.003

Stern, J. V., & Lisiecki, L. E. (2013). North Atlantic circulation and reservoir age changes over the past 41,000 years. *Geophysical Research Letters*, *40*, 3693–3697. https://doi.org/10.1002/grl.50679

Stuiver, M., & Reimer, P. J. (1993). Extended 14C data-base and revised calib 3.0 C-14 age calibration program. *Radiocarbon*, *35*(01), 215–230. https://doi.org/10.1017/S0033822200013904

Tierney, J. E., Pausata, F. S. R., & deMenocal, P. (2016). Deglacial Indian monsoon failure and North Atlantic stadials linked by Indian Ocean surface cooling. *Nature Geoscience*, *9*(1), 46–50. https://doi.org/10.1038/ngeo2603

Ufkes, E., Fred Jansen, J. H., & Brummer, G.-J. A. (1998). Living planktonic foraminifera in the eastern South Atlantic during spring: Indicators of water masses, upwelling and the Congo (Zaire) River plume. *Marine Micropaleontology*, *33*(1–2), 27–53. https://doi.org/10.1016/s0377-8398(97)00032-7

Vinayachandran, P. N., Shankar, D., Vernekar, S., Sandeep, K. K., Amol, P., Neema, C. P., & Chatterjee, A. (2013). A summer monsoon pump to keep the Bay of Bengal salty. *Geophysical Research Letters*, *40*, 1777–1782. https://doi.org/10.1002/grl.50274

Wang, Y., Cheng, H., Edwards, R. L., An, Z. S., Wu, J. Y., Shen, C. C., & Dorale, J. A. (2001). A high-resolution absolute-dated Late Pleistocene monsoon record from Hulu Cave, China. *Science*, *294*(5550), 2345–2348. https://doi.org/10.1126/science.1064618

Weldeab, S., Lea, D. W., Schneider, R. R., & Andersen, N. (2007). 155,000 years of West African monsoon and ocean thermal evolution. *Science*, *316*(5829), 1303–1307. https://doi.org/10.1126/science.1140461

Wu, P., Christidis, N., & Stott, P. (2013). Anthropogenic impact on Earth's hydrological cycle. *Nature Climate Change*, *3*(9), 807–810. https://doi.org/10.1038/nclimate1932

Yao, T., Masson-Delmotte, V., Gao, J., Yu, W., Yang, X., Risi, C., et al. (2013). A review of climatic controls on $\delta^{18}O$ in precipitation over the Tibetan Plateau: Observations and simulations. *Reviews of Geophysics*, *51*, 525–548. https://doi.org/10.1002/rog.20023

Zweng, M. M., Reagan, J. R., Antonov, J. I., Locarnini, R. A., Mishonov, A. V., Boyer, T. P., et al. (2013). World Ocean Atlas 2013, Volume 2: Salinity. In S. Levitus (Ed.), *NOAA Atlas NESDIS* (Vol. 74, 39 pp.). Washington, DC: U.S. Government Printing Office.

References From the Supporting Information

Amidon, W. H., Bookhagen, B., Avouac, J.-P., Smith, T., & Rood, D. (2013). Late Pleistocene glacial advances in the western Tibet interior. *Earth and Planetary Science Letters*, *381*, 210–221. https://doi.org/10.1016/j.epsl.2013.08.041

Bemis, B. E., Spero, H. J., Bijma, J., & Lea, D. W. (1998). Reevaluation of the oxygen isotopic composition of planktonic foraminifera: Experimental results and revised paleotemperature equations. *Paleoceanography*, *13*(2), 150–160. https://doi.org/10.1029/98PA00070

Delaygue, G., Bard, E., Rollion, C., Jouzel, J., StiÈvenard, M., Duplessy, J.-C., & Ganssen, G. (2001). Oxygen isotope/salinity relationship in the northern Indian Ocean. *Journal of Geophysical Research*, *106*(C3), 4565–4574. https://doi.org/10.1029/1999JC000061

Gebregiorgis, D., Hathorne, E. C., Sijinkumar, A. V., Nath, B. N., Nürnberg, D., & Frank, M. (2016). South Asian summer monsoon variability during the last ~54 kyr inferred from surface water salinity and river runoff proxies. *Quaternary Science Reviews*, *138*, 6–15. https://doi.org/10.1016/j.quascirev.2016.02.012

Govil, P., & Naidu, P. (2011). Variations of Indian monsoon precipitation during the last 32 kyr reflected in the surface hydrography of the Western Bay of Bengal. *Quaternary Science Reviews*, *30*(27–28), 3871–3879. https://doi.org/10.1016/j.quascirev.2011.10.004

Gray, W. R., Weldeab, S., Lea, D. W., Rosenthal, Y., Gruber, N., Donner, B., & Fischer, G. (2018). The effects of temperature, salinity, and the carbonate system on Mg/Ca in *Globigerinoides ruber* (white): A global sediment trap calibration. *Earth and Planetary Science Letters*, *482*, 607–620. https://doi.org/10.1016/j.epsl.2017.11.026

Gray, W. R., & Evans, D. (2019). Nonthermal influences on Mg/Ca in planktonic foraminifera: A review of culture studies and application to the last glacial maximum. *Paleoceanography and Paleoclimatology*, *34*, 306–315. https://doi.org/10.1029/2018PA003517

Heyman, J., Stroeven, A. P., Caffee, M. W., Hättestrand, C., Harbor, J. M., Li, Y., et al. (2011). Palaeoglaciology of Bayan Har Shan, NE Tibetan Plateau: Exposure ages reveal a missing LGM expansion. *Quaternary Science Reviews*, *30*(15-16), 1988–2001. https://doi.org/10.1016/j.quascirev.2011.05.002

Kudrass, H. R., Hofmann, A., Doose, H., Emeis, K., & Erlenkeuser, H. (2001). Modulation and amplification of climatic changes in the Northern Hemisphere by the Indian Summer Monsoon during the past 80 k.y. *Geology*, *29*(1), 63–66. https://doi.org/10.1130/0091-7613(2001)029<0063:maaocc>2.0.co;2

Marzin, C., Kallel, N., Kageyama, M., Duplessy, J. C., & Braconnot, P. (2013). Glacial fluctuations of the Indian monsoon and their relationship with North Atlantic climate: New data and modelling experiments. *Climate of the Past*, *9*(5), 2135–2151. https://doi.org/10.5194/cp-9-2135-2013

Midhun, M., Lekshmy, P. R., & Ramesh, R. (2013). Hydrogen and oxygen isotopic compositions of water vapor over the Bay of Bengal during monsoon. *Geophysical Research Letters*, *40*, 6324–6328. https://doi.org/10.1002/2013GL058181

Panmei, C., Naidu, P. D., & Mohtadi, M. (2017). Bay of Bengal exhibits warming trend during the Younger Dryas: Implications of AMOC. *Geochemistry, Geophysics, Geosystems*, *18*, 4317–4325. https://doi.org/10.1002/2017GC007075

Rashid, H., England, E., Thompson, L., & Polyak, L. (2011). Late Glacial to Holocene Indian Summer Monsoon Variability Based upon Sediment Records Taken from the Bay of Bengal, Terrestrial. *Atmospheric & Oceanic Sciences*, *22*(2), 215–228. https://doi.org/10.3319/TAO.2010.09.17.02(TibXS)

Saraswat, R., Lea, D. W., Nigam, R., Mackensen, A., & Naik, D. K. (2013). Deglaciation in the tropical Indian Ocean driven by interplay between the regional monsoon and global teleconnections. *Earth and Planetary Science Letters*, *375*, 166–175. https://doi.org/10.1016/j.epsl.2013.05.022

Tierney, J. E., & Tingley, M. P. (2018). BAYSPLINE: A new calibration for the alkenone Paleothermometer. *Paleoceanography and Paleoclimatology*, *33*, 281–301. https://doi.org/10.1002/2017PA003201

Waelbroeck, C., Labeyrie, L., Michel, E., McManus, J., Lambeck, K., Balbon, E., & Labracherie, M. (2002). Sea-level and deep water temperature changes derived from benthic foraminifera isotopic records. *Quaternary Science Research*, *21*, 295–305.